

A discussion of 2D induced polarization effects in airborne electromagnetic and inversion with a robust 1D laterally constrained inversion scheme

Changhong Lin¹, Gianluca Fiandaca², Esben Auken², Marco Antonio Couto³, and Anders Vest Christiansen²

ABSTRACT

Recently, the interest in the induced polarization (IP) phenomenon in airborne time-domain electromagnetic (ATEM) data has increased considerably. IP may affect the ATEM data significantly and mask underlying geologic structures. To simulate 2D airborne IP data, a 2D finite-element forward-modeling algorithm has been developed with the dispersive conductivity described by the well-known Cole-Cole model. We verify our algorithm by comparison with the 1D solution of the AarhusInv code. Two-dimensional forward responses on six synthetic models, mimicking archetypal 2D conductive and chargeable anomalies, have been generated, and the results indicate that 2D IP affects the data significantly. Differences between the 2D IP responses and the 1D IP responses are evident above the 2D anomalies and at their edges. These

differences are similar to what is found when comparing 2D and 1D forward responses over conductive 2D anomalies without considering IP. We evaluate an effective robust inversion scheme to recover the 2D IP parameters using the 1D laterally constrained inversion (LCI) scheme. The inversion of the synthetic data using the robust scheme indicates that not only can the IP parameters be recovered, but also the IP inversions can provide more accurate resistivity sections than a resistivity-only inversion, in terms of resistivity values and anomaly thickness/depth. The field example from Hope Bay area in Canada is even more valuable, considering that part of the profile consists of only negative data, which cannot be inverted with a resistivity-only scheme. Furthermore, the edge effects at the anomaly boundaries are less pronounced in the IP parameters than in the resistivity parameter on the synthetic models with more conductive backgrounds.

INTRODUCTION

The induced polarization (IP) phenomenon in airborne electromagnetic (AEM) data presents a problem to exploration in many parts of the world. It is a well-known phenomenon and since [Smith and Klein \(1996\)](#) first demonstrate the presence of IP effects, which have been further discussed by several authors (e.g., [Marchant et al., 2014](#); [Macnae, 2016](#); [Kaminski and Viezzoli, 2017](#)). The advances in electronic and data processing especially for airborne time-domain electromagnetic (ATEM) systems have led to a much larger decay time recording and better signal-to-noise ratios, which in turn have revealed that IP is a severe problem and cannot be neglected during modeling.

[Kozhevnikov and Antonov \(2008, 2010\)](#) discuss numerical experiments exploring the potentialities and limitations in the 1D IP inversion of ground-based transient electromagnetic responses of a uniform and a two-layer earth. [Kratzer and Macnae \(2012\)](#) develop an approximate interpretation tool to invert ATEM IP responses. [Fiandaca et al. \(2012\)](#) present a laterally constrained 1D inversion scheme to model the complex resistivity in terms of the Cole-Cole IP model ([Cole and Cole, 1941](#); [Pelton et al., 1978](#)), and [Viezzoli et al. \(2017\)](#) use the approach of [Fiandaca et al. \(2012\)](#) to study the recovering of IP parameters from AEM data. [Kang and Oldenburg \(2016\)](#) and [Kang et al. \(2017\)](#) propose a 3D inversion method for ATEM IP data, where they do a 3D resistivity only in-

Manuscript received by the Editor 11 February 2018; revised manuscript received 14 September 2018; published ahead of production 05 December 2018; published online 12 February 2019.

¹China University of Geosciences (Beijing), School of Geophysics and Information Technology, Beijing, China. E-mail: linchh@cugb.edu.cn (corresponding author).

²Aarhus University, Hydrogeophysics Group, Department of Geoscience, Aarhus, Denmark. E-mail: gianluca.fiandaca@geo.au.dk; esben.auken@geo.au.dk; anders.vest@geo.au.dk.

³CPRM — Geological Survey of Brazil, Sao Paulo, Brazil. E-mail: marco.couto@cprm.gov.br.

© 2019 Society of Exploration Geophysicists. All rights reserved.

version of the early time data not significantly affected by IP, subtract the forward responses from the data and by this decouple the IP model from the resistivity model. However, the computation power involved is significant for a 3D inversion and the decoupling approach neglects the correlations between the resistivity and the IP parameters (by assuming that the early-time data are not affected by IP).

Two-dimensional forward modeling of ATEM IP has, to the best of our knowledge, not been presented before, and we use it to gain insight into IP responses over 2D chargeable bodies and to develop a robust inversion scheme. We have developed a 2D finite-element (FE) modeling algorithm for ATEM data, where the model is defined in two dimensions and the source is a finite rectangular loop. To simulate airborne IP data, our 2D forward code uses the resistivity Cole-Cole (RCC) parameterization (Cole and Cole, 1941; Pelton et al., 1978) and the maximum phase angle (MPA) reparameterization of the RCC model (Fiandaca et al., 2018) to compute the electrical complex resistivity (MacLennan et al., 2014).

As described in Auken et al. (2008), 1D inversion of ATEM data in a 3D environment is possible and gives a good recovery of the true model in many cases. Nevertheless, even in one dimension, the ATEM IP inversion is significantly ill-posed and it is a challenging problem to recover the four parameters simultaneously. Here, a robust inversion scheme, based on the multiparametric 1D laterally constrained inversion (LCI) scheme (Auken and Christiansen, 2004), is proposed and tested on the 2D data. The inversion scheme relies on 1D forward/Jacobian computations, but without any decoupling approximations, i.e., with a simultaneous recovery of the resistivity and the IP parameters. In addition to the standard 1D LCI scheme described in Auken et al. (2015), several modifications are introduced to improve the robustness of the inversion process.

The inversion results of the synthetic data from the 2D models and of a field example are used to illustrate the effectiveness of the robust inversion scheme, which suggests a way forward for IP inversion of large-scale field data sets for geophysical exploration and geologic mapping.

METHODOLOGY

In this section, we will describe the steps involved in the investigation, i.e., (1) the 2D modeling, (2) the system description and simulation of noise, (3) the robust inversion scheme, and (4) the synthetic models and sounding layout.

2D modeling

For simulating ATEM data, we developed a 2D modeling algorithm. In the implementation, the source is a horizontal rectangular loop. To deal with the singularity of the field at the source location, an approach separating the total electric (EM) and magnetic fields into a primary part containing the singularity and a secondary part (Wannamaker et al., 1986; Unsworth et al., 1993; Newman and Alumbaugh, 1995) is used. The EM fields generated by a horizontal electric dipole at the earth's surface on either a uniform whole space or a layered half-space can be evaluated using the expressions presented by Ward and Hohmann (1987). By integrating numerically around the loop using the transverse electric (TE) mode of these expressions and some modifications of the reflection coefficients, the primary EM fields above the earth generated by a horizontal rectangular loop in the air on either a uniform whole space or a

layered half-space can be obtained in the wavenumber (k_y) domain. The FE method is then applied to the numerical modeling of the secondary field for each k_y .

Assuming a harmonic time dependence of $e^{i\omega t}$, the secondary electric field \mathbf{E}^s and magnetic field \mathbf{H}^s are described by Maxwell's equations:

$$\nabla \times \mathbf{E}^s = -i\mu_0\omega\mathbf{H}^s, \quad (1)$$

$$\nabla \times \mathbf{H}^s = \sigma\mathbf{E}^s + \sigma_a\mathbf{E}^p, \quad (2)$$

where \mathbf{E}^p is the primary electric field, ω is the angular frequency, μ_0 is the vacuum magnetic permeability (permeability variations are not considered), σ is the complex conductivity, $\sigma_a = \sigma - \sigma_p$ is the anomalous complex conductivity, and σ_p is the background conductivity used for computing the primary field. To include the IP phenomenon in the Maxwell's equation, the RCC model as in Pelton et al. (1978) is applied to model the dispersive complex conductivity in equation 2:

$$\sigma(\omega) = \frac{1}{\rho_0 \left[1 - \frac{m_0}{10^3} \left(1 - \frac{1}{1+(i\omega\tau_p)^C} \right) \right]}, \quad (3)$$

with four interconnected parameters: ρ_0 is the electrical resistivity (ohm-m), m_0 is the intrinsic chargeability (mV/V), τ_p is the relaxation time (s), and C is the frequency exponent.

Following Mitsuhashi (2000), we can obtain two coupled governing differential equations for the secondary electric field \hat{E}_y^s and magnetic field \hat{H}_y^s in the k_y -domain after the Fourier transform is applied to equations 1 and 2 with respect to y . The other components \hat{E}_x^s , \hat{E}_z^s , \hat{H}_x^s , and \hat{H}_z^s are calculated from the spatial derivatives of \hat{E}_y^s and \hat{H}_y^s . To derive the finite-element equations, the Galerkin method (Zienkiewicz, 1977) and a rectangular element with four nodes have been adopted. The simple Dirichlet condition $\hat{E}_y^s = \hat{H}_y^s = 0$ at the boundaries is assigned. We solve the linear system equations by the Bi-CGSTAB method (Smith, 1996; Lin et al., 2018) to obtain \hat{E}_y^s and \hat{H}_y^s . The total EM fields in the k_y -domain are transformed to the space domain by the inverse Fourier transformation. The ATEM responses are obtained by transforming the total EM fields from the frequency domain to the time domain.

To assess modeling accuracy of the 2D code, the time derivatives of the vertical magnetic fields, $d\mathbf{B}/dt$, were compared with the 1D solution implemented in the AarhusInv code (Auken et al., 2015). The comparison between the 1D solution of the AarhusInv code and the 2D response on a three-layer model is shown in Figure 1. The three-layer model consists of a homogeneous background ($\rho_0 = 5000 \Omega\text{m}$, $m_0 = 0 \text{ mV/V}$), with an anomalous layer ($\rho_0 = 500 \Omega\text{m}$, $m_0 = 350 \text{ mV/V}$, $\tau_p = 0.001 \text{ s}$, $C = 0.5$) embedded in it at a depth of 20 m. The consistency of the 2D response and the 1D solution is sufficiently accurate, with 6.4% maximum deviation at the gates close to the sign change and less than 2% at all others.

System description and noise: Synthetic example

The main features of the ATEM system used to simulate synthetic data are described in Table 1. Two types of errors are considered when constructing the noise model (Auken et al., 2008): (1) a uni-

form relative error, which simulates possible inaccuracy in the system description and (2) a contribution that depends on the signal level, which mimics the background random noise. Consequently, the total noise contribution to synthetic data is described as

$$v = G(0,1) \cdot [\text{STD}_{\text{uni}}^2 + v_{\text{noise}}^2]^{\frac{1}{2}}, \quad (4)$$

where $G(0,1)$ is the Gaussian distribution with zero mean and standard deviation 1, $\text{STD}_{\text{uni}}^2$ is the uniform noise, and v_{noise}^2 is the background noise contribution. Here, the uniform STD is set to 3% on all the time gates. The background noise can be approximated to a straight line with a slope of $t^{-1/2}$ in a log-log plot. From field data, we estimated an empirical value for the background noise of 10^{-9} V/m⁴, at 1 ms (Auken et al., 2008).

In the plots throughout the paper, the data are presented in volts (V) normalized by the receiver and transmitter areas (m⁴), but not by current and turns of the transmitter loop. This normalization is chosen to highlight the level of the signal in comparison with the background noise.

1D LCI robust scheme

To invert the synthetic data, we use the 1D LCI approach, which minimizes an objective function that includes 2D lateral constraints on the model parameters belonging to neighboring stations. The objective function is expressed by

$$Q = \left(\frac{\delta \mathbf{d}^T \mathbf{C}_{\text{obs}}^{-1} \delta \mathbf{d} + \delta \mathbf{r}^T \mathbf{C}_R^{-1} \delta \mathbf{r}}{N_d + N_R} \right)^{\frac{1}{2}}, \quad (5)$$

where \mathbf{C}_{obs} and \mathbf{C}_R are the data and constraint covariance matrices; $\delta \mathbf{d} = (\mathbf{d} - \mathbf{d}_{\text{obs}})$ represents the difference between the forward response \mathbf{d} and the observed data \mathbf{d}_{obs} ; $\delta \mathbf{r} = -\mathbf{R}\mathbf{m}$ is the roughness of the model vector \mathbf{m} , computed through the roughness matrix \mathbf{R} ; N_d and N_R represent the number of data points and roughness constraints. A Gauss-Newton style minimization scheme with a Marquardt modification (Marquardt, 1963) is applied to find the set of model parameters that minimize the L_2 -misfit with respect to observed data and regularization (and prior information, if present). The model parameters are log-transformed for reducing their dynamic range. The stopping criterion for the inversion is enforced on the relative change in the objective function between consecutive iterations and is set to 1%. More details about the LCI scheme can be found in Auken and Christiansen (2004) and Auken et al. (2015). In this study, we inverted all the soundings along a profile simultaneously to minimize a common objective function including lateral constraints. The 1D LCI algorithm is robust to 2D earth structures due to the lateral constraints (Auken et al., 2008), but edge effects

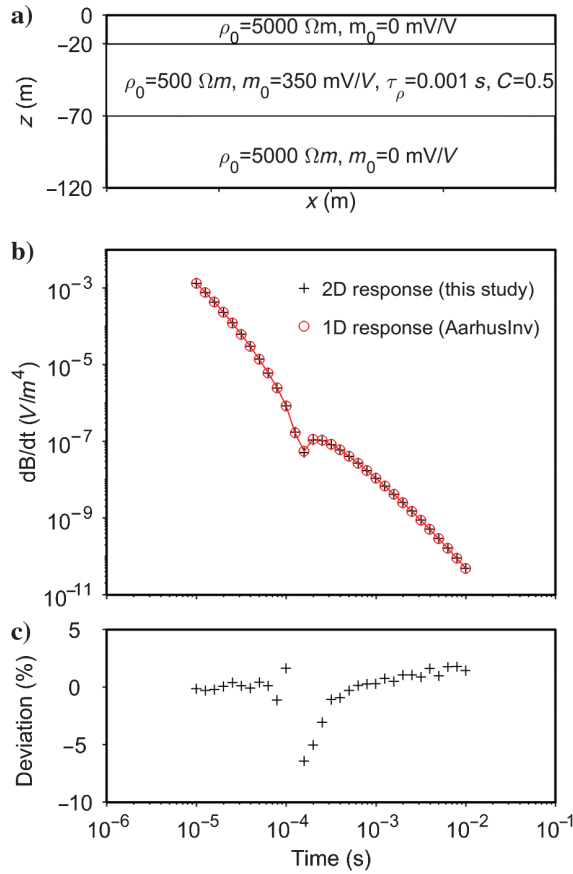


Figure 1. Comparison between the 1D solutions of the AarhusInv code and the 2D responses on a three-layer model. (a) The three-layer model. (b) The time derivatives of the vertical magnetic fields. (c) Deviations of our 2D solutions from AarhusInv's 1D solutions.

Table 1. Synthetic AEM system parameters description.

| Parameter | | Value | |
|-------------|--------------------------------|------------------------|--|
| Transmitter | Number of transmitter turns | 16 | |
| | Transmitter area | 300 m ² | |
| | Peak current | 100 A | |
| | Peak moment | 480,000 NIA | |
| | Turn-on time | -10 ms | |
| | Ramp up to peak current time | -9 ms | |
| | Turn-off time | 0 μ s | |
| | Ramp down to zero current time | 5 μ s | |
| | Receiver | Number of output gates | 31 |
| | | Time-gates interval | From 10 μ s to 10 ms (10 gates/decade) |

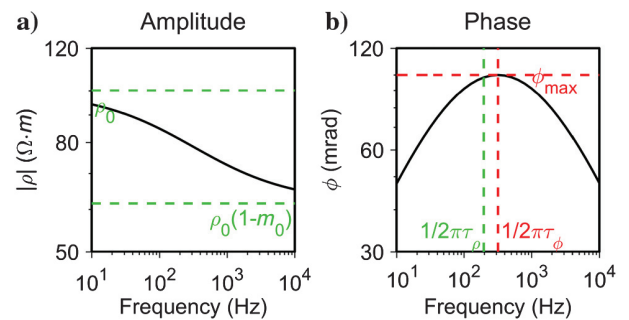


Figure 2. (a) Amplitude and (b) phase of the Cole-Cole complex conductivity spectrum for the model $m_{\text{MPA}} = \{\rho_0 = 100 \Omega m, \phi_{\text{max}} = 100 \text{ mrad}, \tau_\phi = 5 \times 10^{-4} \text{ s}, C = 0.5\}$. The low- and high-frequency limits of the amplitude are ρ_0 and $\rho_0(1 - m_0)$ (with m_0 expressed in V/V).

such as “pants legs,” that are reminiscent of diffraction hyperbolas from seismic sections (Wolfgram et al., 2003), may be found in the 1D LCI inversion models when significant lateral resistivity contrasts are present. The 1D LCI has its advantages in the reduction of the nonuniqueness, recovering the lateral continuity of the inverted model, compared with individual sounding-by-sounding 1D inversions. Finally, compared with a full 2D inversion, the 1D LCI is computationally efficient, which makes field-data inversion practical.

Compared with the standard 1D LCI scheme described in Auken et al. (2015) and used in Viezzoli et al. (2017) and Kaminski and Viezzoli (2017), five modifications have been implemented to increase the stability and parameter recovery of the ATEM IP inversion: (1) The model space has been reparameterized to minimize parameter correlations, (2) a method to establish robust starting models has been identified, (3) the τ and C parameters have been fixed in the first few iterations awaiting structure to happen in the resistivity and chargeability parameters, (4) the data standard deviations have been modified close to the sign change to improve convergence, and (5) the damping scheme has been modified to balance the multiparameter model space better. In the following, these five modifications are treated in detail.

Model space

The model reparameterization consists of the MPA reparameterization of the RCC model introduced by Fiandaca et al. (2018) for

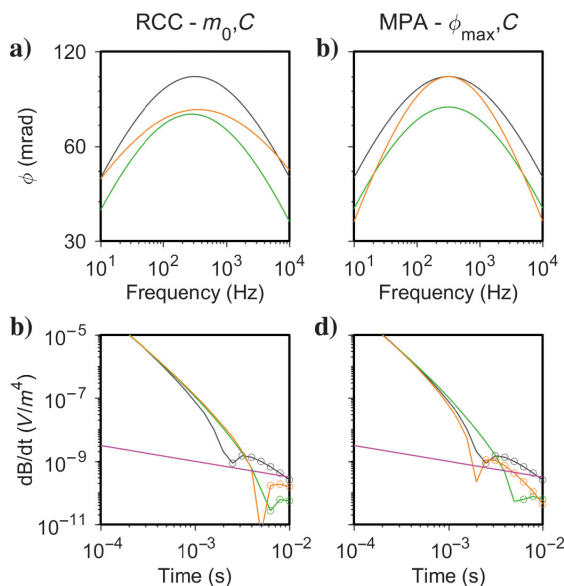


Figure 3. Phase spectra and AEM responses for the homogeneous half-space models. Reference model: $m_{\text{MPA}} = \{\rho_0 = 100 \Omega\text{m}, \varphi_{\text{max}} = 100 \text{ mrad}, \tau_\varphi = 5 \times 10^{-4} \text{ s}, C = 0.5\}$. (a) Reference phase spectrum (gray line), spectrum obtained with 20% m_0 decrease (green line) and 20% C decrease (orange line) for the RCC model. (b) Reference AEM response (gray line), response obtained with 20% m_0 decrease (green line) and 20% C decrease (orange line) for the RCC model. (c) Reference phase spectrum (gray line), spectrum obtained with 20% φ_{max} decrease (green line) and 20% C increase (orange line) for the MPA model. (d) Reference AEM response (gray line), response obtained with 20% φ_{max} decrease (green line) and 20% C increase (orange line) for the MPA model. In sections (b and d), the circled data are negative. The magenta lines represent the noise level.

galvanic, ground-based frequency-domain and time-domain IP inversions, described by the parameters

$$\mathbf{m}_{\text{MPA}} = \{\rho_0, \varphi_{\text{max}}, \tau_\varphi, C\}, \quad (6)$$

where φ_{max} represents the MPA of the Cole-Cole complex resistivity and τ_φ is the inverse of the frequency at which φ_{max} is reached. Figure 2 shows the absolute value and the phase (sign reversed) of the Cole-Cole complex resistivity as a function of frequency, with the classic Cole-Cole parameters (ρ_0, m_0, τ_ρ), and φ_{max} and τ_φ represented as well. The phase reaches the maximum φ_{max} at the frequency $1/2\pi\tau_\varphi$. The terms τ_φ and τ_ρ are linked through the relation $\tau_\varphi = \tau_\rho \cdot (1 - m_0)^{1/2C}$.

In the inversion of galvanic, ground-based time-domain, or frequency-domain spectral IP data, the m_0 and C parameters of the RCC model are strongly correlated (Bérubé et al., 2017; Fiandaca et al., 2018), whereas the correlation between φ_{max} and C in the MPA parameterization is weaker, leading to a significantly better resolution of φ_{max} compared with m_0 (Fiandaca et al., 2017). A reduction of the $\varphi_{\text{max}} - C$ correlation in comparison with the $m_0 - C$ correlation is obtained also for ATEM data. This can be seen in Figure 3, in which the phase of the complex resistivity and the ATEM response of a homogeneous half-space are compared when varying the φ_{max}/C parameters of the MPA model and the m_0/C parameters of the classic RCC model. In Figure 3a, the phase of the reference RCC model (gray line) is compared with the phase obtained with a 20% decrease of m_0 (green line) and a 20% decrease of C (orange line). The decrease of m_0 and the decrease of C cause

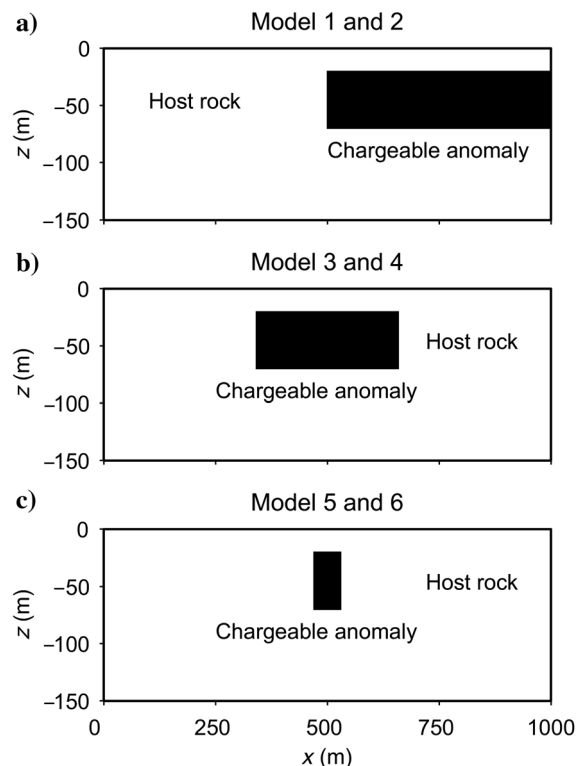


Figure 4. The three basic 2D experimental models. The horizontal lengths of anomalies are (a) infinite, (b) 320 m, and (c) 60 m. By applying two sets of IP parameters to the anomalies, a total of six models are achieved.

similar phase variations close to the phase peak. This similarity in the phase variation is reflected into the effect on the ATEM response (Figure 3b), where the responses are practically indistinguishable (green and orange lines) above the background noise. In Figure 3c, the phase of the MPA reference model (gray line) is compared with the phase obtained with a 20% decrease of φ_{\max} (green line) and a 20% increase of C (orange line). Here, it is an increase instead of decrease because a C decrease would bring the orange line even farther from the phase of 20% φ_{\max} decrease. The spectra obtained with the 20% φ_{\max} decrease and the 20% C increase are significantly different close to the phase peak, and the corresponding ATEM responses (Figure 3d) are clearly distinguishable.

Robust starting models

Like any other ill-posed problem, the IP inversion problem can become unstable and sensitive to the starting parameter values. Compared with inverting for resistivity only, the choice of the starting values for the four parameters becomes significantly more critical in IP inversion. As presented by Viezzoli et al. (2017), the use of ancillary a priori information (drilling, geology, ground geophysics, etc.) can help to reduce the ambiguity of the inversion results. The question is how to choose the starting parameter values without available ancillary information, which is the normal situation. Our tests found that using starting values close to the values of the half-space host rock (i.e., ignoring an anomalous IP layer) is a good choice for all four MPA Cole-Cole parameters. If the starting value of ρ_0 or φ_{\max} is far away from the values of the host rock, the inversion often converges to the wrong model. Based on this, and considering that the host rock is usually nonchargeable, our robust scheme to choose the starting MPA Cole-Cole parameters is (1) invert resistivity-only including only the nonnegative data, and using tight lateral and vertical constraints, to get a nearly homogeneous resistivity model as the starting value for ρ_0 ; (2) choose a low or moderate value (10–30 mrad) as the starting φ_{\max} , which does not trigger negative data (note that smaller values are needed when starting from high resistivity values and that the values depend also on the system characteristics, so that forward modeling tests might be needed for finding appropriate values); (3) set the starting value for C to 0.3, i.e., an intermediate value; (4) select a value in the interval 1e-1s to 1e-5s, which triggers the strongest IP as the starting values for τ_φ . This choice for the starting resistivity is based on the assumption that the IP-affected AEM data are only present in a portion of the profile/area and that the remaining soundings can give a reasonable estimate of the background resistivity. This is not necessarily always true, and the negative data can dominate not only spatially in the surveyed area, but also within each sounding. In this case, the resistivity of the starting model can be hard to retrieve automatically and it has to be manually set.

Locking parameters

Simultaneous recovery of four parameters increases the non-uniqueness of the inversion. To favor the structure in the ρ_0 and φ_{\max} parameters and decrease nonuniqueness, the robust scheme is separated into two steps after the starting model is determined. In step one, the parameters τ_φ and C are fixed for several iterations,

focusing the structure to ρ_0 and φ_{\max} . Then, in step two, τ_φ and C are released and all four parameters are optimized simultaneously.

Sign changes

During the iterative inversion process, changes in model parameters that impact the timing of the sign reversal in the forward responses infer large variation in the data misfit of the objective function. This leads to instability in the inversion process, which easily traps the model in a local minimum. To mitigate the effects linked to the sign change, we increase the uniform STD at the four time gates (two positive and two negative) around the sign change (s) from 3% to 30%.

Table 2. The two different MPA Cole-Cole parameters used in the 2D experimental models.****

| | | ρ_0 (Ωm) | m_0 (mV/V) | φ_{\max} (mrad) | τ_ρ (s) | τ_φ (s) | C |
|--------|-----------|-------------------------------|--------------|-------------------------|-----------------|--------------------|-----|
| Type 1 | Host rock | 100 | 10 | 0.4 | 0.01 | 0.01 | 0.1 |
| | Anomaly | 10 | 500 | 142 | 0.001 | 0.0005 | 0.5 |
| Type 2 | Host rock | 5000 | 0 | 0 | 0 | 0 | 0 |
| | Anomaly | 500 | 350 | 89 | 0.001 | 0.00065 | 0.5 |

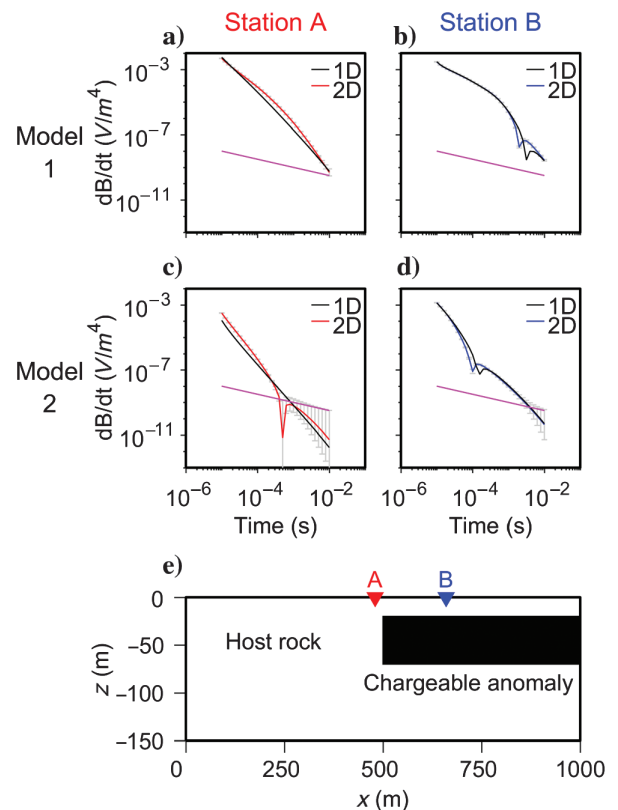


Figure 5. Comparison between the 2D responses (red and blue lines with gray error bar) and the 1D response (black lines) at stations A (red) and B (blue) generated on models (a and b) 1 and (c and d) 2. The magenta lines represent the noise level. Stations A and B lie at 480 and 660 m in the x -direction, respectively.

Damping scheme

The adaptive damping approach based on the Marquardt method described in Auken et al. (2015) damps all the inversion parameters through the maximum diagonal element of the matrix $\mathbf{G}_n^T \mathbf{C}'^{-1} \mathbf{G}_n'$, where \mathbf{G}_n' and \mathbf{C}' are the Jacobian of the n th iteration and the data covariance matrix, respectively (extended to also contain the prior and roughness information; for details, see Auken et al., 2015). In the IP inversion, we have four inversion parameters per layer, which means that the magnitudes of the Jacobian elements differ significantly. For example, the τ_φ parameter usually has very small derivative values compared with the other parameters. This means that the damping scheme described in Auken et al. (2015) likely overdamps the weakly resolved parameter types, impeding their variation through the inversion process. To overcome this problem, the damping scheme was modified to evaluate the maximum of the $\mathbf{G}_n^T \mathbf{C}'^{-1} \mathbf{G}_n'$ matrix block-wise for each parameter type and damping them per block.

Altogether, the effect of the robust LCI scheme facilitates a robust convergence of the ATEM IP inversions, as shown in the “Results” section.

Synthetic models and sounding layout

Fifty-one synthetic soundings simulating a profile length of 1 km (20 m sounding spacing) were used for each of the 2D forward modeling scenarios. In the 2D finite-element forward modeling,

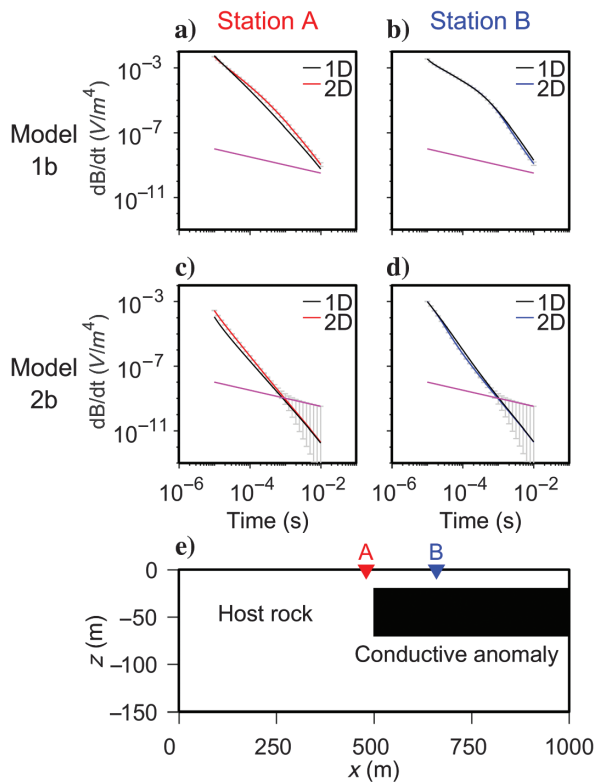


Figure 6. Comparison between the 2D responses (the red and blue lines with the gray error bar) and the 1D response (black lines) at stations A (red) and B (blue) generated on conductive models (a and b) 1b and (c and d) 2b, which have the same conductivity structure as models 1 and 2, but without an IP effect ($\varphi_{\max} = 0$ mrad). The magenta lines represent the noise level. Stations A and B lie at 480 and 660 m in the x -direction, respectively.

the grid has a fine central part containing the model, the transmitter, and receivers laterally and vertically. The grid has 141×39 in the x - z plane (a total of 5499 nodes). A nominal flight height of 30 m over a flat surface was used.

In our experiments, we consider six 2D models based on three base models. The models are displayed in Figure 4, and they all consist of a chargeable anomaly 20 m below surface. The chargeable and relatively conductive anomalies are embedded in a homogeneous and nonchargeable host rock, mimicking ore bodies. The lengths of the chargeable anomaly blocks are infinite (models 1 and 2), 320 (models 3 and 4) and 60 m (models 5 and 6). Two different sets of IP parameters (shown in Table 2) are used in the models. The Cole-Cole parameters of type 2 are the same used for the disseminated sulfide model by Viezzoli et al. (2017, Figure 2). Models using the type 2 parameters are comparatively resistive. We also consider a comparatively conductive type 1 with different IP parameters. In our six experimental models, the type 1 Cole-Cole parameters are used for models 1, 3, and 5 and the type 2 are used for models 2, 4, and 6.

RESULTS

Synthetic examples

2D effects on AEM IP data

Comparisons between the 2D responses (the red and blue lines with the gray error bar) and the 1D responses (the black lines) at station A (red) and station B (blue) generated on models 1 and 2 are

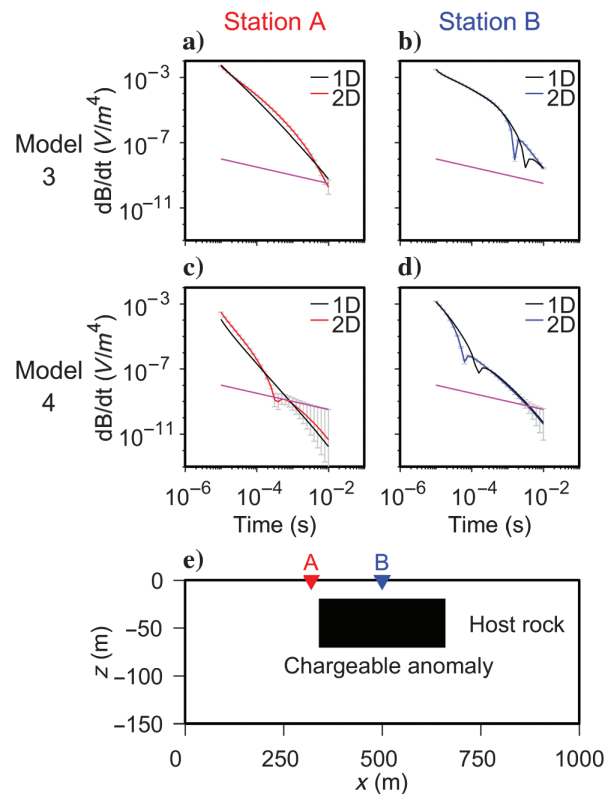


Figure 7. The same as Figure 5 but for models (a and b) 3 and (c and d) 4. Stations A and B lie at 320 and 500 m in the x -direction, respectively.

shown in Figure 5a and 5b and Figure 5c and 5d, respectively. Influenced by the edge of the target, significant differences between the 2D responses and 1D responses are observed at the A station (Figure 5a and 5c), which is 20 m outside the anomaly. A sign change due to the 2D effect is seen only with the comparatively resistive model 2 (Figure 5c), although the negative data are below the noise level. Edge effects are still seen at station B, 160 m away from the anomaly edge, whereas they are negligible at 440 m from the edge (not shown).

On model 2, stronger IP effects with a much earlier sign reversal is observed at station B (Figure 5d). Similarly, on model 1, clear sign changes appear at station B (Figure 5b). The differences in the timing of the sign reversal are an effect of the relative size between the signal coming from the anomalous conductivity and the negative effect of the anomalous chargeability. To underline this, Figure 6 shows a comparison of the 2D and 1D responses on models 1b and 2b, which have the same conductivity structure as models 1 and 2, but without IP ($\phi_{max} = 0$ mrad). Here, 2D effects are present at stations A and B, but no sign reversals are observed. Hence, the sign reversal is an effect solely of the IP response, but the timing includes a balance with the conductivity-driven signal.

Figure 7 shows the comparison between the 2D responses and the 1D responses at stations A and B generated on models 3 and 4. Stations A and B are again 20 and 160 m away from the target edge. The 2D responses at stations A and B have obvious differences to the 1D responses and have similar characteristics as those in Figure 5 although the IP effects on models 3 and 4 are stronger, seen as a sign reversal at an earlier time.

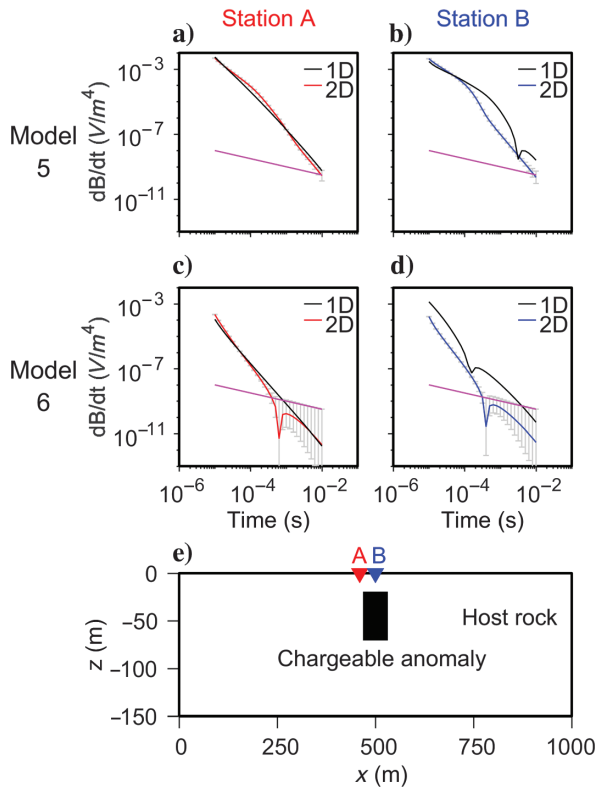


Figure 8. The same as Figure 5 but for models (a and b) 5 and (c and d) 6. Stations A and B lie at 460 and 500 m in the x -direction, respectively.

The comparisons between the 2D and 1D responses at stations A and B for models 5 and 6 are shown in Figure 8. The 2D responses generated by the comparatively smaller anomaly in the x -direction (models 5 and 6) are still different from the 1D responses. Looking at the 2D responses alone, there are significant differences between models 5 and 6, where model 5 does not produce a sign change, whereas model 6 creates a clear sign reversal. However, the negative data for model 6 are below the noise level. Such responses with no sign change or negative data below the noise level would be hard to interpret as IP effects.

Comparing the responses at station B on model 3 and those on model 5, which have the same Cole-Cole parameters but different model geometry, the 2D responses are obviously affected by the length of the target. A clearer sign reversal is seen because the longer target (model 3, Figure 7b) is charged up more strongly. A similar phenomenon is observed in the 2D responses at station B on models 4 and 6 (Figures 7d and 8d).

Figure 9 shows a comparison between the 2D IP responses and the 2D resistivity-only responses at station A (from Figures 5a, 5c,

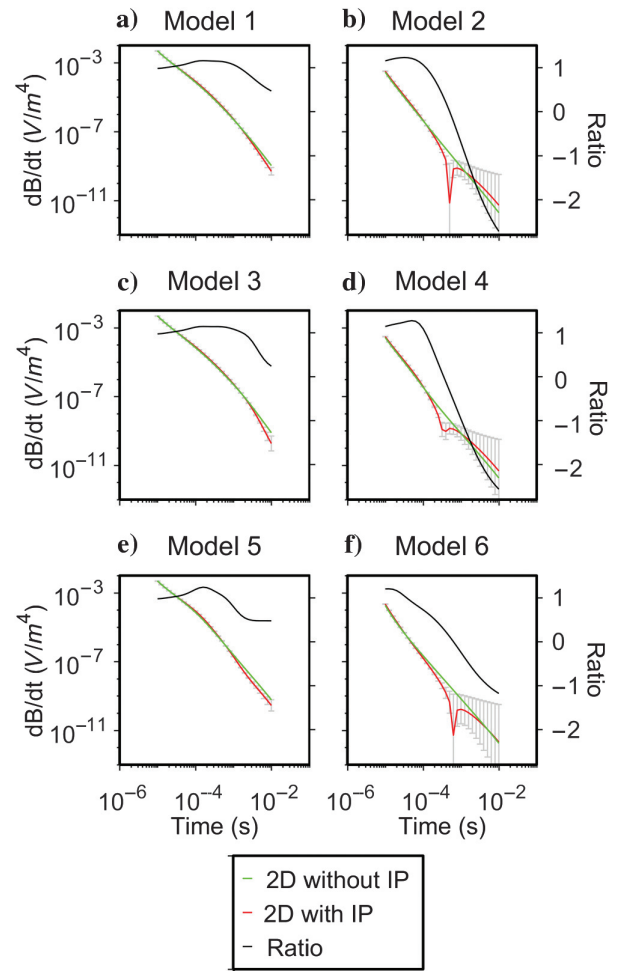


Figure 9. Comparison between the 2D IP responses (the red lines with the gray error bar) and the 2D resistivity-only responses (green lines) at station A (shown in Figures 5, 7, and 8) generated on the (a) models 1, (b) 2, (c) 3, (d) 4, (e) 5, and (f) 6. The black lines show the ratio of the 2D IP responses divided by 2D resistivity-only responses.

7a, 7c, 8a, and 8c) for all six models. The black lines show the ratios of the 2D IP responses normalized by 2D resistivity-only responses. The negative ratios come from the negative values of the IP responses at late gate times for models 2, 4, and 6. The responses are similar at the early gate times, with ratios close to 1, but the differences become significant at later times. For models 1, 3, and 5, the (logarithmic) average deviations between the 2D IP responses and the 2D resistivity-only responses are 18%, 24%, and 32%, respectively, with the larger deviations at approximately 10 ms (the smallest ratio is 0.24 for model 1). For models 2, 4, and 6, the deviations are much larger than for the conductive models because sign reversals are present in the 2D IP responses, the smallest ratio being 0.013 for model 2 at the time gate of 0.5012 ms. Consequently, big 2D IP edge effects are present when the background is resistive and sign reversals exist in the 2D IP responses, but significant edge effects are also present when sign reversals are not observed.

Inversion results

First, inversions with the robust 1D inversion scheme on the synthetic data from the six experimental models without noise contamination are presented. The robust scheme uses the following settings: MPA inversion; starting ρ_0 from the resistivity-only inversion without negative data, $\varphi_{\max} = 30$ mrad, $\tau_\varphi = 1e - 4$ s, and $C = 0.3$; τ_φ

and C locked for the first seven iterations; increased STD to 30% at the four gate times at the sign reversal; and the adaptive damping approach.

Figure 10 shows the inversion results from the synthetic data for models 1, 3, and 5 (Figure 10a, 10b, and 10c, respectively). The depth of investigation (DOI) is computed following Fiandaca et al. (2015). The anomalies of the three models are recovered for all four MPA parameters, in magnitude and shape, and the data are well-fitted. This means that the differences between the 1D and 2D responses seen in the synthetic studies are compensated in the inversion through small parameter variations that do not prevent the recovery of reasonable models. However, pants-leg edge effects are present in the resistivity and MPA (φ_{\max}) sections. The edge effects in the φ_{\max} parameter are a consequence of the 2D IP effects at the anomaly edges presented in Figure 9. The edge effects are present in φ_{\max} and not in τ_φ and C because φ_{\max} controls the strength of the IP effect in the data more than τ_φ and C . However, contrary to the resistivity parameter, the edge effects in φ_{\max} lay below the DOI on models 1 and 3. On model 5, the φ_{\max} edge effects are above the DOI, but the φ_{\max} values retrieved by the inversion are smaller in the edges than in the anomaly. On the contrary, on model 5, the resistivity edge effects are as strong as the resistivity anomaly.

To investigate the effect of inverting with a full IP model with four parameters, we show 1D resistivity-only inversion results of

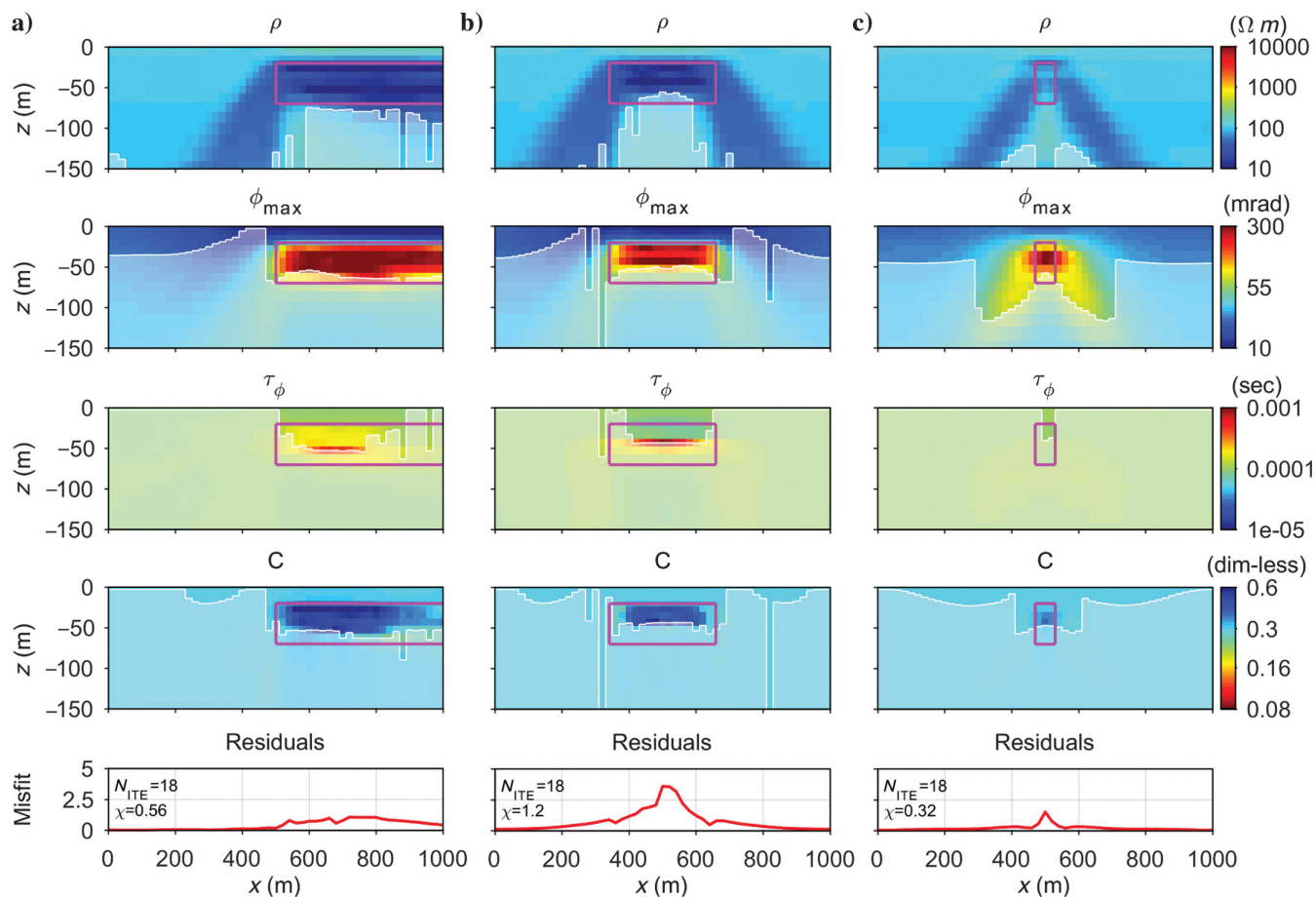


Figure 10. Inversion results from 1D LCI of the synthetic data for models 1 (a), 3 (b), and 5 (c) using the robust scheme. The shaded areas represent the portions of the models below the DOI.

the synthetic data for models 1, 3, and 5 in Figure 11. To do this, the negative data have been removed. As is clearly seen, the resistivity-only inversions do not reproduce the resistivity models as well and they have a poorer data fit.

Figure 12 shows the inversion results from the synthetic data for models 2, 4, and 6 using the robust 1D inversion scheme. The anomalies of the three models are decently recovered in the resistivity and phase sections, but not as well as in Figure 10. Furthermore, contrary to Figure 10, in Figure 12, the edge effects in ϕ_{\max} are above the DOI and similar to the resistivity edge effects because the 2D IP edge effects in the forward data are stronger

in the models with more resistive backgrounds (Figure 9). The inversion results from the synthetic data inverting resistivity-only after deleting the negative data are shown in Figure 13. It is found that the inversions for models 2 and 4 represent the anomalies at a much shallower depth than the true depth. Nevertheless, compared with the results obtained from inverting resistivity only (Figure 13), the IP inversions have smaller data misfits and more accurate resistivity images (the first row in Figure 12). As shown in Figure 8c and 8d, there are no IP effects above the noise level in the 2D responses from by the smallest anomaly in model 6. Therefore, the inversions for model 6 cannot predict the true model.

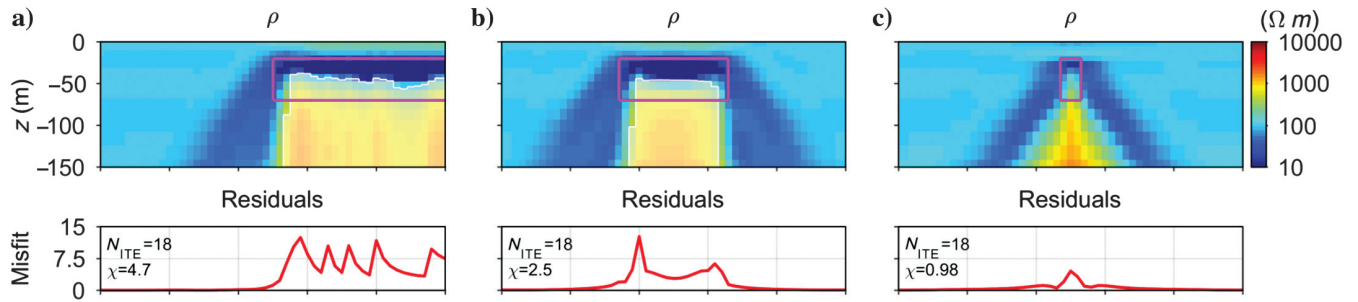


Figure 11. Inversion results from 1D LCI of the synthetic data for models 1 (a), 3 (b), and 5 (c) inverting resistivity only and without considering the negative data. The shaded areas represent the portions of the models below the DOI.

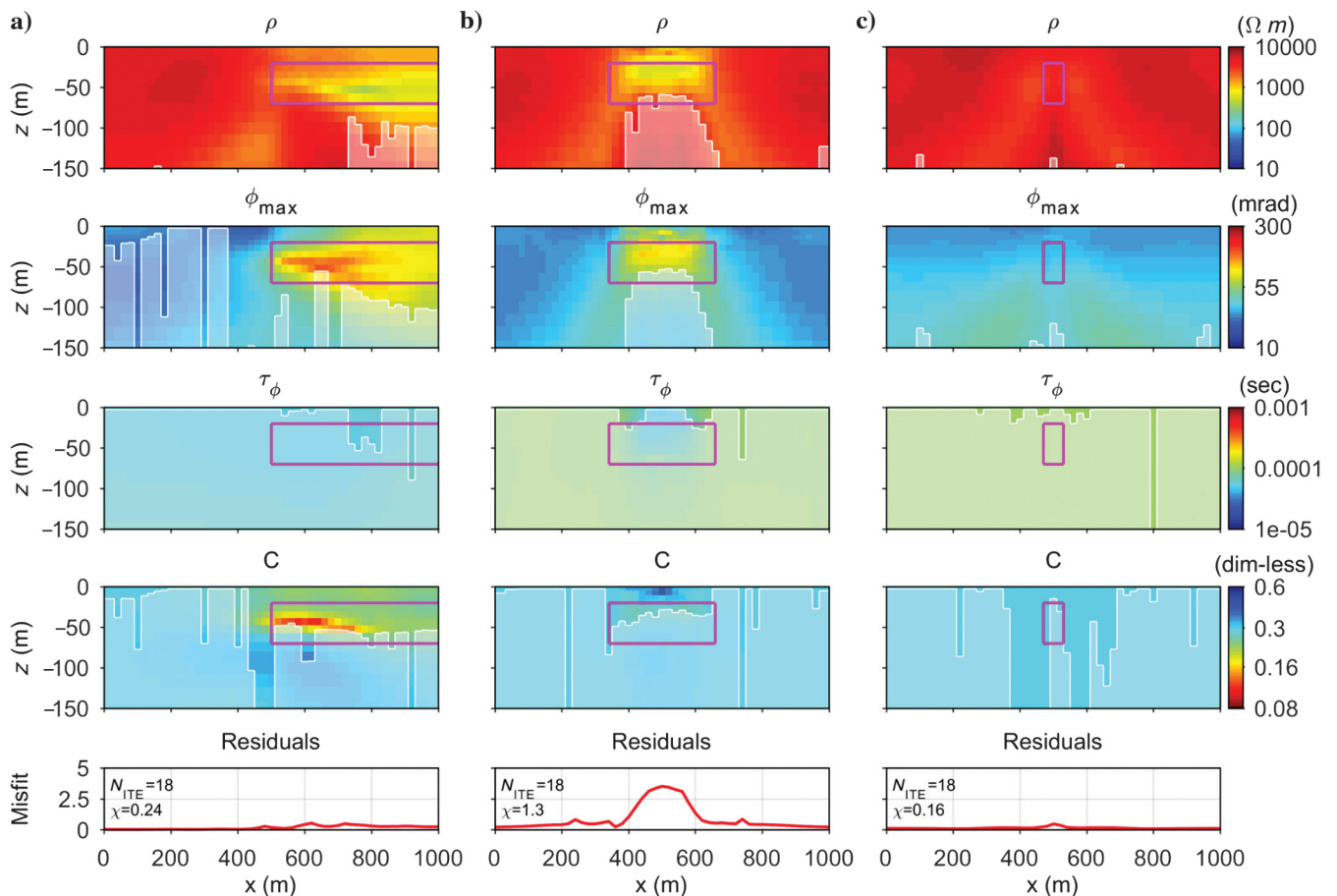


Figure 12. Inversion results from 1D LCI of the synthetic data for models 2 (a), 4 (b), and 6 (c) using the robust scheme. The shaded areas represent the portions of the models below the DOI.

To highlight the role of the robust inversion scheme in the results, we have carried out separate inversions with the elements of the robust scheme taken out one by one. The results are shown in Figure 14. These inversions are presented against the data misfits of the MPA inversions with the full robust scheme (black lines) for all six experimental models. In Figure 14a, the red line shows the data misfits of the inversions without the robust starting model for resistivity, where a homogeneous starting value $\rho_0 = 700 \Omega\text{m}$ is used instead. The data misfits without robust starting ρ_0 are generally larger than those using the robust scheme (black line) except for model 4. In Figure 14b, the blue line shows the data misfits of the inversions without the robust STD values (a 30% STD at the four time gates

at the sign reversal). The misfits without the robust noise are larger than the misfits of the inversion with the robust scheme, except for model 6, for which there is a small decrease. In Figure 14c, the green line shows the data misfits without locking τ_ϕ and C in the first seven iterations. Again, the misfits are generally bigger especially for the models 1–3. In Figure 14d, the magenta line shows the data misfits of the inversion without the parameter-type dependent damping scheme, with a significant misfit increase for models 1 and 2; whereas models 3 and 4 show a decreased misfit. For the few models where the robust scheme does not give an improved data residual, we evaluated the model results with the general conclusion that the inversion results with robust scheme are more accurate

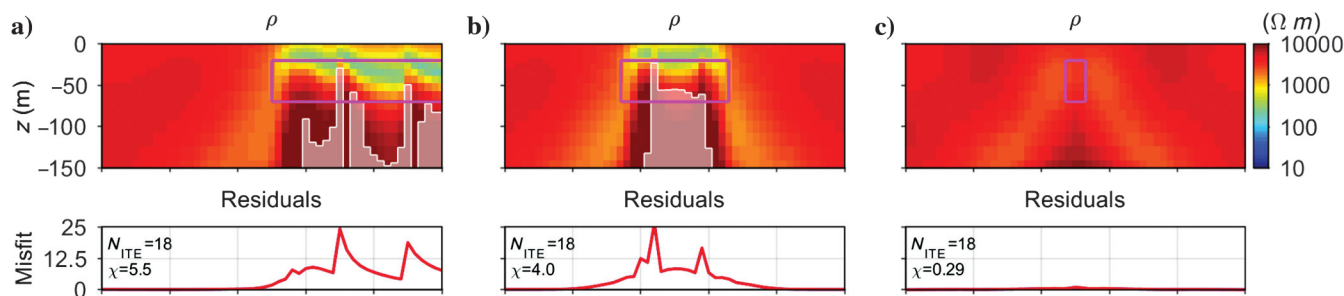


Figure 13. Inversion results from 1D LCI of the synthetic data for models 2 (a), 4 (b), and 6 (c) inverting resistivity only and without considering the negative data. The shaded areas represent the portions of the models below the DOI.

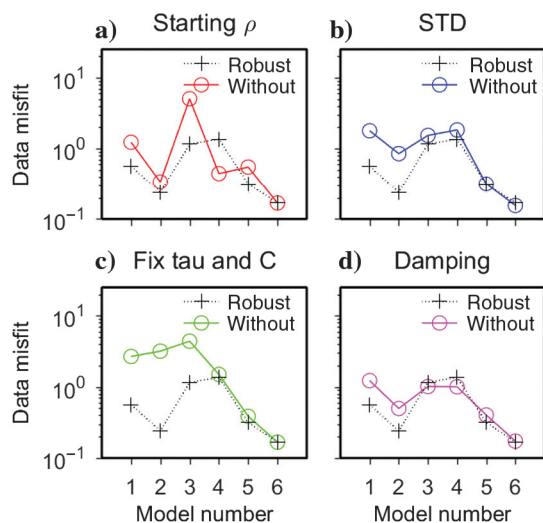


Figure 14. Comparison between the data misfits of the inversions for six experimental models (without noise contamination) with the robust scheme (black lines) and those without using it (colored lines). (a) The red line shows the data misfits of the inversions without the robust starting ρ_0 (i.e., with starting $\rho_0 = 700 \Omega\text{m}$ for all inversions). (b) The blue line shows the data misfit of the inversion without robust STD values (i.e., without the increased STD around the sign reversal). (c) The green line shows the data misfit of the inversion without fixing τ_ϕ and C in the first seven iterations. (d) The magenta line shows the data misfit of the inversion without the parameter-type dependent damping scheme.

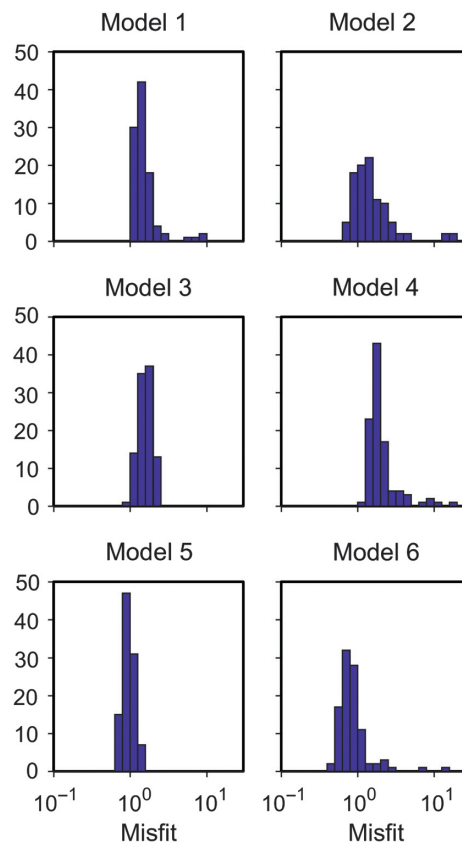


Figure 15. The distribution of the data misfits from the 100 inversions of the synthetic data with 100 different random noise contaminations for six models, using the robust scheme.

representations of the true model, but we are not showing these results for brevity. Moreover, the inversion results obtained without any of the implementations of the robust scheme are significantly worse than those presented in Figure 14.

Finally, to test the robust scheme against noise contaminated data, 100 data sets contaminated with different random noise distributions were inverted for each experimental model. Figure 15 shows the distribution of the data misfits from the 100 inversions for six models. A good data misfit, approximately 1, is obtained for the most part of the inversions. Furthermore, the inversion models are very similar to those shown in Figures 10 and 12.

Field example

The survey

The field example is extracted from a SkyTEM survey over the Hope Bay area, in the West Kitikmeot region of Nunavut Territory, Canada. The study area presents several world-class porphyry-type gold deposits in a greenstone belt environment, in particular, Doris, Madrid, and Boston deposits, all TMAC Resources Inc. properties. The survey was requested by TMAC and covered 12,123 km in the Madrid deposit area. Its main purpose was to add relevant geologic information to the understanding of the gold-deposit environment.

Due to the mineralization styles and as described in Kaminski et al. (2016), it is expected to have a significant IP effect in this AEM survey. In fact, these authors demonstrated that this data set needs to be inverted considering a multiparameter IP mode, to recover a reliable resistivity model and avoid distorted conductive anomalies when a resistivity-only parameterization is considered.

Taking in account these characteristics, this data set is ideal for the application of the proposed robust inversion scheme.

Kaminski et al. (2016) point out three conductive anomalies in the north portion of the SkyTEM survey, which were significantly distorted when a resistivity-only model was applied, but were better recovered using a multiparametric IP inversion (they used the RCC parameterization). In this work, we present the results for the proposed robust inversion scheme applied for a cut in a flight line profile with 3.2 km extension in the region of an anomaly given number three.

AEM system

The system used for the field example was the SkyTEM516, with dual magnetic dipole moments: low moment (LM) and high moment (HM). The key parameters for the transmitter and receiver systems are summarized in Table 3 (adapted from the SkyTEM ApS survey report). The nominal terrain clearance for the transmitter/receiver system is 30 m, flight speed of 87 km/h and the nominal sampling rate is 10 Hz, after preliminary processing during the survey execution.

Inversion results

In Figure 16a and 16b, the LM and HM AEM data of the field example are presented, respectively. The blue marks represent the positive data, the red marks represent the negative data, whereas the gray marks show the data removed during processing (with some portions of the profile in which all data are below the noise floor due to a very resistive ground). The chosen profile presents negative

Table 3. SkyTEM516 system parameters used in the Hope Bay survey (adapted from SkyTEM ApS survey report).

| Parameter | | Value | |
|-------------|---|----------------------------|------------------------------|
| | | LM | HM |
| Transmitter | Number of transmitter turns | 2 | 16 |
| | Transmitter area | 536.36 m ² | |
| | Peak current | 5.3/5.3 A | 113.8/117.9 A |
| | Peak moment | 4500 NIA | 1,000,000 NIA |
| | Repetition frequency | 210 Hz | 30 Hz |
| | Turn-on time | -800.000 μs | -400.000 μs |
| | Ramp up to peak current time | 0 ms | -0.3766 ms |
| | Turn-off time | 1.776 μs | 0 ms |
| | Ramp down to zero current time | 29.050 μs | 705.013 μs |
| | Duty cycle | 33% | 24% |
| Receiver | Waveform | Square | |
| | Sample rate | All decays were measured | |
| | Number of output gates | 28 | 39 |
| | Time gates interval (calibrated gate center referenced to the LM turn-off time) | From 54.115 to 1369.615 μs | From 172.615 to 10275.615 μs |
| | Receiver coil low-pass filter | 210 kHz | |
| | Receiver instrument low-pass filter | 300 kHz | |
| | Repetition frequency | 210 Hz | 30 Hz |
| | Front gate | 0.0 μs | 800 μs |

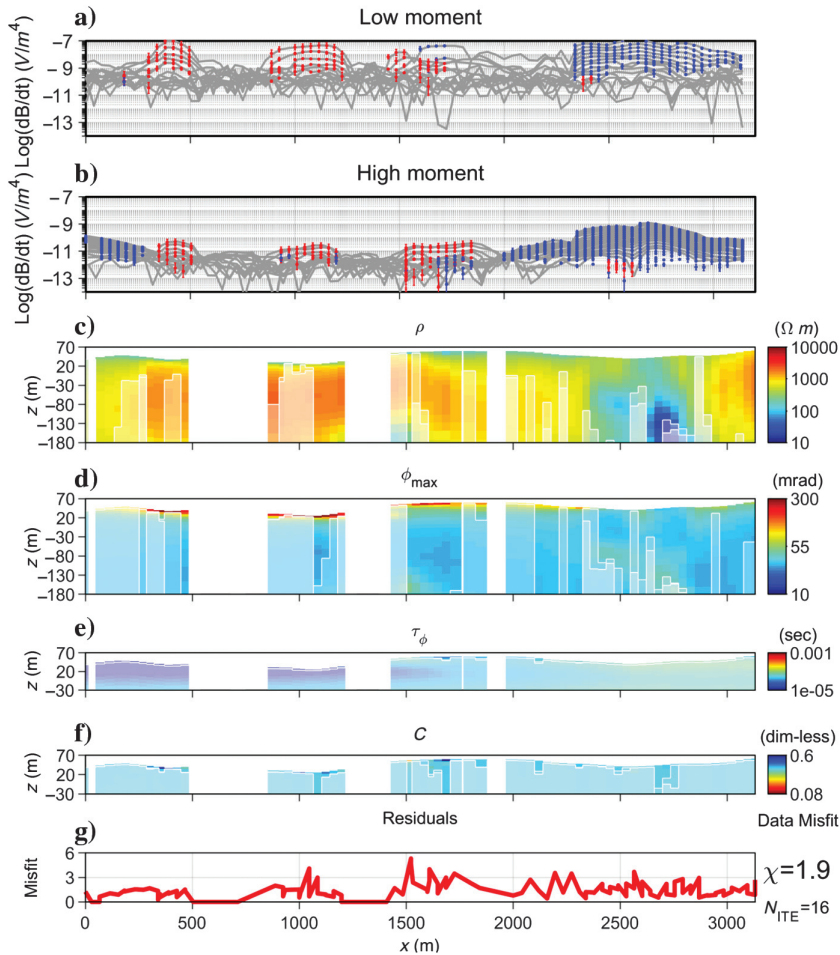


Figure 16. Data and inversion model of the field profile. (a and b) LM and HM data. The blue and red marks indicate the positive and negative data (and error bars) used in the inversion. The gray lines represent all measured data, including the data points removed during processing because of no earth signal. (c–f) Inversion sections for the ρ_0 , ϕ_{\max} , τ_{ϕ} , and C parameters. The shaded areas represent the portions of the models below the DOI. (g) Misfit section.

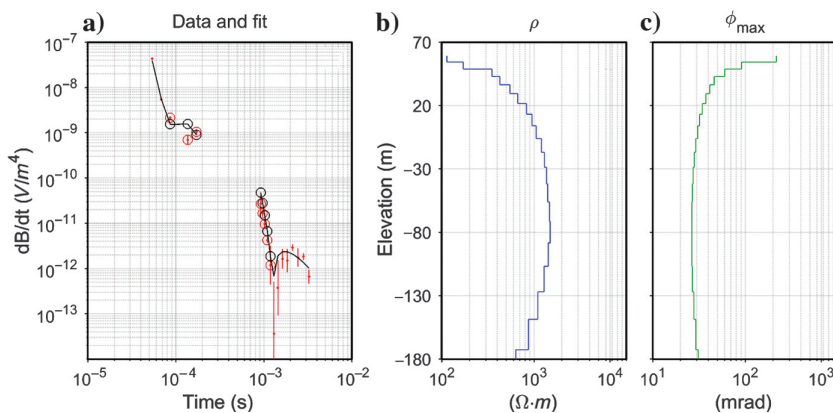


Figure 17. Example of data, fit, and corresponding model. (a) Data (red marks) and forward response (black line and marks); negative measured/forwarded data are circled. (b) Resistivity model. (c) MPA model.

data in the LM and HM acquisitions, not only at late times (as in the synthetic examples) but also at early times, with full-negative AEM responses (above the noise floor) as well as responses starting negative, increasing to positive values, and finally decaying to zero.

The inversion results for the ρ_0 , ϕ_{\max} , τ_{ϕ} , and C parameters are presented in Figure 16c–16f, and the corresponding data misfit is presented in Figure 16g. The figure sections of the τ_{ϕ} and C parameters (Figure 16e and 16f) are plotted with a smaller depth range because the DOI is really shallow and no significant information is present in the deep part of the sections. Figure 17a shows a sounding example with data fit, with the corresponding 1D model used for generating the forward response presented in Figure 17b–17c.

The inversion results presented in Figures 16 and 17 were computed using the same robust setting of the synthetic examples, except for the starting resistivity value. Indeed, the resistivity-only inversion carried out on the positive data with tight lateral and vertical constraints give a too-resistive starting model, which prevents a good convergence of the inversion. Consequently, a homogeneous value equal to 250 Ωm was used as the starting value for the inversion.

The inversion model presents a shallow conductive and chargeable layer in a significant portion of the profile. This layer is responsible of the early-time negative data, and it makes an interpretation of the data in terms of a resistivity-only inversion impossible. Deeper conductive anomalies are present in the west portion of the profile, associated with moderate values in the ϕ_{\max} section. The inversion in terms of the MPA model allows us to fit almost all the negative data present in the section, as evidenced by the example in Figure 17a.

CONCLUSION

Based on the FE method and the Cole-Cole model, a 2D modeling algorithm has been developed to simulate ATEM IP data, and it is verified against the 1D AarhusInv solution. Using the modeling code, we generated 2D ATEM forward responses on six experimental models and studied the 2D IP effects on ATEM data. For inversion, a robust 1D LCI scheme for ATEM IP is presented, based on five new implementations: (1) using the MPA reparameterization of the Cole-Cole model, which decreases parameter correlations; (2) identification of a general robust starting model; (3) fixing of the τ and C parameters for the first few iterations; (4) definition of data standard deviations that facilitate convergence, especially around possible sign changes; and (5) a new parameter-type dependent damping scheme.

From the comparison of the 2D IP responses, 1D IP responses, and 2D responses without IP, it is concluded that 2D IP edge effects are clearly present in the forward data. The magnitude of the 2D IP edge effects depends on the horizontal length of the 2D target and the distance between the receiver and the target, as well as on the four MPA Cole-Cole parameters, with stronger edge effects on models with more resistive backgrounds. Furthermore, 2D responses with no sign change or negative data below the noise level are generated by the short target in the horizontal direction, and they would be hard to interpret as IP effects.

Two-dimensional synthetic data on six models were inverted. The inversion results show that it is possible to recover the 2D IP parameters using a 1D scheme, but pants-leg edge effects are present in the inversion models when large parameter contrasts exist. However, the 2D IP edge effects are less pronounced than the resistivity edge effects on models with more conductive backgrounds. Overall, the anomalies of the models that generate strong IP signals are well-resolved. Equally important, inverting with IP parameters, contrary to resistivity-only inversion, results in better defined resistivity sections. In other words — if data exhibiting IP effects are inverted ignoring the IP parameters, one will get erroneous resistivity models as a result. These considerations are corroborated by the inversion of a field example in which full-negative decays are present in many areas of the profile, making resistivity-only inversion impossible. However, incorporating IP parameters in the model description makes inversion possible with realistic resistivity structures of the subsurface and well-fitted data.

ACKNOWLEDGMENTS

This study has been jointly supported by the National Natural Science Foundation of China (grant nos. 41674134 and 41874159), National Key Research and Development Program of China (grant nos. 2016YFC0601104 and 2017YFC0602204), State Scholarship Fund of China, and the Special Fund for Basic Scientific Research of Central Colleges. The paper is also a part of the water center and the AirTech4water Innovation Fund Denmark project. Constructive comments by P. Leroy, two anonymous referees, the associate editor X. Garcia, and the assistant editor J. Shragge significantly improved this manuscript and are greatly appreciated. Also, the authors would like to thank SkyTEM ApS and TMAC Resources Inc. to provide and allow access to the SkyTEM data set used in the field example in this work.

DATA AND MATERIALS AVAILABILITY

Data associated with this research are available and can be obtained by contacting the corresponding author.

REFERENCES

- Auken, E., and A. Christiansen, 2004, Layered and laterally constrained 2D inversion of resistivity data: *Geophysics*, **69**, 752–761, doi: [10.1190/1.1759461](https://doi.org/10.1190/1.1759461).
- Auken, E., A. V. Christiansen, L. H. Jacobsen, and K. I. Sørensen, 2008, A resolution study of buried valleys using laterally constrained inversion of TEM data: *Journal of Applied Geophysics*, **65**, 10–20, doi: [10.1016/j.jappgeo.2008.03.003](https://doi.org/10.1016/j.jappgeo.2008.03.003).
- Auken, E., A. Christiansen, C. Kirkegaard, G. Fiandaca, C. Schamper, A. Behroozmand, A. Binley, E. Nielsen, F. Effersø, N. Christensen, K. Sørensen, N. Foged, and G. Vignoli, 2015, An overview of a highly versatile forward and stable inverse algorithm for airborne, ground-based and borehole electromagnetic and electric data: *Exploration Geophysics*, **46**, 223–235, doi: [10.1071/EG13097](https://doi.org/10.1071/EG13097).
- Bérubé, C. L., M. Chouteau, P. Shamsipour, R. J. Enkin, and G. R. Olivo, 2017, Bayesian inference of spectral induced polarization parameters for laboratory complex resistivity measurements of rocks and soils: *Computers and Geosciences*, **105**, 51–64, doi: [10.1016/j.cageo.2017.05.001](https://doi.org/10.1016/j.cageo.2017.05.001).
- Cole, K. S., and R. H. Cole, 1941, Dispersion and absorption in dielectrics. I: Alternating current characteristics: *The Journal of Chemical Physics*, **9**, 341–351, doi: [10.1063/1.1750906](https://doi.org/10.1063/1.1750906).
- Fiandaca, G., E. Auken, A. Christiansen, and A. Gazoty, 2012, Time-domain-induced polarization: Full-decay forward modeling and 1D laterally constrained inversion of Cole-Cole parameters: *Geophysics*, **77**, no. 3, E213–E225, doi: [10.1190/geo2011-0217.1](https://doi.org/10.1190/geo2011-0217.1).
- Fiandaca, G., A. Christiansen, and E. Auken, 2015, Depth of investigation for multi-parameters inversions: Presented at the Near Surface Geoscience 21st European Meeting of Environmental and Engineering Geophysics.
- Fiandaca, G., L. M. Madsen, and P. K. Maurya, 2018, Re-parameterization of the Cole-Cole model for improved spectral inversion of induced polarization data: *Near Surface Geophysics*, **16**, 385–399, doi: [10.3997/1873-0604.2017065](https://doi.org/10.3997/1873-0604.2017065).
- Kaminski, V., and A. Viezzoli, 2017, Modeling induced polarization effects in helicopter time-domain electromagnetic data: Field case studies: *Geophysics*, **82**, no. 2, B49–B61, doi: [10.1190/geo2016-0103.1](https://doi.org/10.1190/geo2016-0103.1).
- Kaminski, V., A. Viezzoli, and A. Menguini, 2016, Case studies: Hope Bay gold deposits: *Aarhus Geophysics*.
- Kang, S., D. Fournier, and D. Oldenburg, 2017, Inversion of airborne geophysics over the DO-27/DO-18 kimberlites. Part 3: Induced polarization: *Interpretation*, **5**, no. 3, T327–T340, doi: [10.1190/INT-2016-0141.1](https://doi.org/10.1190/INT-2016-0141.1).
- Kang, S., and D. W. Oldenburg, 2016, On recovering distributed IP information from inductive source time domain electromagnetic data: *Geophysical Journal International*, **207**, 174–196, doi: [10.1093/gji/ggw256](https://doi.org/10.1093/gji/ggw256).
- Kozhevnikov, N. O., and E. Y. Antonov, 2008, Inversion of TEM data affected by fast-decaying induced polarization: Numerical simulation experiment with homogeneous half-space: *Journal of Applied Geophysics*, **66**, 31–43, doi: [10.1016/j.jappgeo.2008.08.001](https://doi.org/10.1016/j.jappgeo.2008.08.001).
- Kozhevnikov, N. O., and E. Y. Antonov, 2010, Inversion of IP-affected TEM responses of a two-layer earth: *Russian Geology and Geophysics*, **51**, 708–718, doi: [10.1016/j.rgg.2010.05.011](https://doi.org/10.1016/j.rgg.2010.05.011).
- Kratzer, T., and J. Macnae, 2012, Induced polarization in airborne EM: *Geophysics*, **77**, no. 5, E317–E327, doi: [10.1190/geo2011-0492.1](https://doi.org/10.1190/geo2011-0492.1).
- Lin, C., H. Tan, W. Wang, T. Tong, M. Peng, M. Wang, and W. Zeng, 2018, Three-dimensional inversion of CSAMT data in the presence of topography: *Exploration Geophysics*, **49**, 253–267, doi: [10.1071/EG16067](https://doi.org/10.1071/EG16067).
- MacLennan, K., M. Karaoulis, and A. Revil, 2014, Complex conductivity tomography using low-frequency crosswell electromagnetic data: *Geophysics*, **79**, no. 1, E23–E38, doi: [10.1190/geo2012-0531.1](https://doi.org/10.1190/geo2012-0531.1).
- Macnae, J., 2016, Quantifying airborne induced polarization effects in helicopter time domain electromagnetics: *Journal of Applied Geophysics*, **135**, 495–502, doi: [10.1016/j.jappgeo.2015.10.016](https://doi.org/10.1016/j.jappgeo.2015.10.016).
- Marchant, D., E. Haber, and D. Oldenburg, 2014, Three-dimensional modeling of IP effects in time-domain electromagnetic data: *Geophysics*, **79**, no. 6, E303–E314, doi: [10.1190/geo2014-0060.1](https://doi.org/10.1190/geo2014-0060.1).
- Marquardt, D., 1963, An algorithm for least-squares estimation of nonlinear parameters: *Journal of the Society for Industrial and Applied Mathematics*, **11**, 431–441, doi: [10.1137/0111030](https://doi.org/10.1137/0111030).
- Mitsuhata, Y., 2000, 2-D electromagnetic modeling by finite-element method with a dipole source and topography: *Geophysics*, **65**, 465–475, doi: [10.1190/1.1444740](https://doi.org/10.1190/1.1444740).
- Newman, G. A., and D. L. Alumbaugh, 1995, Frequency-domain modeling of airborne electromagnetic responses using staggered finite differences: *Geophysical Prospecting*, **43**, 1021–1042, doi: [10.1111/j.1365-2478.1995.tb00294.x](https://doi.org/10.1111/j.1365-2478.1995.tb00294.x).
- Pelton, W., S. Ward, P. Hallof, W. Sill, and P. Nelson, 1978, Mineral discrimination and removal of inductive coupling with multifrequency IP: *Geophysics*, **43**, 588–609, doi: [10.1190/1.1440839](https://doi.org/10.1190/1.1440839).
- Smith, J., 1996, Conservative modeling of 3-D electromagnetic fields. Part II: Biconjugate gradient solution and an accelerator: *Geophysics*, **61**, 1319–1324, doi: [10.1190/1.1444055](https://doi.org/10.1190/1.1444055).
- Smith, R., and J. Klein, 1996, A special circumstance of airborne induced-polarization measurements: *Geophysics*, **61**, 66–73, doi: [10.1190/1.1443957](https://doi.org/10.1190/1.1443957).
- Unsworth, M., B. Travis, and A. Chave, 1993, Electromagnetic induction by a finite electric dipole source over a 2-D earth: *Geophysics*, **58**, 198–214, doi: [10.1190/1.1443406](https://doi.org/10.1190/1.1443406).
- Viezzoli, A., V. Kaminski, and G. Fiandaca, 2017, Modeling induced polarization effects in helicopter time domain electromagnetic data: Synthetic case studies: *Geophysics*, **82**, no. 2, E31–E50, doi: [10.1190/geo2016-0096.1](https://doi.org/10.1190/geo2016-0096.1).

- Wannamaker, P., J. Stodt, and L. Rijo, 1986, Two-dimensional topographic responses in magnetotellurics modeled using finite elements: *Geophysics*, **51**, 2131–2144, doi: [10.1190/1.1442065](https://doi.org/10.1190/1.1442065).
- Ward, S. H., and G. W. Hohmann, 1987, 4. Electromagnetic theory for geophysical applications, in M. N. Nabighian and J. D. Corbett, eds., *Electromagnetic methods in applied geophysics — Theory*: SEG, 131–312.
- Wolfgram, P., D. Sattel, and N. B. Christensen, 2003, Approximate 2D inversion of AEM data: *Exploration Geophysics*, **34**, 29–33, doi: [10.1071/EG03029](https://doi.org/10.1071/EG03029).
- Zienkiewicz, O. C., 1977, *The finite element method*, 3rd ed.: McGraw-Hill.